RSC Advances

PAPER

View Article Online
View Journal | View Issue

Cite this: *RSC Adv.*, 2026, **16**, 23129

Investigation of the structural, optical and electrical properties of $ZnAl_2O_4$

Amira Bougoffa, *[a] Ala Eddin Mabrouki,[a] Adel Benali,[a] Essebti Dhahri,[a] Abderrazek Oueslati[b] and B. F. O. Costa[c]

Received 16th February 2026
Accepted 14th April 2026

DOI: 10.1039/d6ra01381c

rsc.li/rsc-advances

This work presents an investigation into the structural, optical, and electrical properties of $ZnAl_2O_4$ powder. The synthesis of this material was performed *via* an auto-combustion route. Then, structural characterization was carried out by XRD followed by Rietveld refinement of the obtained pattern, which indicates a normal spinel structure with the $Fd\bar{3}m$ space group, known as the Gahnite structure. This result was confirmed using RAMAN spectra recorded at room temperature, which exhibited two peaks corresponding to the Eg and T2g modes. After that, TEM microscopy proved the presence of semi-spherical particles with a size of about 45 nm. The optical properties from the PL emission spectra exhibit multicolor emission that can be attributed to defects and vacancies in the material. The electrical measurements of the prepared $ZnAl_2O_4$ sample prove the existence of semiconductor behavior following the Jonscher law at higher frequencies. At low frequencies, the dc conduction process was governed by the VRH process, while at high temperature it was assisted by the SPH mechanism.

1. Introduction

In the last few years, oxide-based materials, such as spinel and perovskite materials, have attracted a lot of attention due to their interesting properties and multifunctional behavior.[1,2] As a result, they have been used for several applications, such as catalysts, photosynthesis, laser and fluorescent materials and sensors.[3–6] However, an important compromise is usually discussed concerning the structural stability and reproducibility of these materials because of the high number of factors affecting their properties. This family of materials has the general formula AB_2O_4 (A is a bivalent metal cation occupying the tetrahedral site, and B is a trivalent cation, occupying the octahedral site) and exhibits a stable $Fd\bar{3}m$ cubic structure, mainly the one named Gahnite.[7–12] In particular, aluminate luminescent materials have attracted a lot of attention regarding their stable crystal structure, good cationic distribution and excellent optical and dielectric properties.[13–15] The structural stability of these materials is usually accompanied by instability of the optical and dielectric properties. In this context, several investigations have focused on the synthesis and characterization of luminescent spinel zinc aluminate, where the physical properties depend strongly on the synthesis route. This compound is known generally as a semiconductor material with a wide band gap at room temperature ($E_g \approx 3.5$–3.9 eV).[16,17] Furthermore, its tunable optical bandgap and photoluminescence efficiency represent important factors for its application in phosphors, light-emitting devices, and photocatalysis.[18–21] These properties can be enhanced by aliovalent or isovalent substitution of Zn or Al by transition metals or rare-earth elements. Indeed, Shangpan Huang *et al.*[22] synthesized Mn-doped $ZnAl_2O_4$ by a hydrothermal route, and proved that a variation in the preparation process can modify the optical properties of this material through the appearance of a peak in the near-infrared region. In contrast, V. N. Adoons *et al.*[23] proved that only a UV emission band was exhibited by Fe-doped $ZnAl_2O_4$ prepared by the Pechini sol–gel synthesis route. However, the cited synthesis techniques present some disadvantages, such as complex operating procedures, long reaction and treatment times, and high annealing temperatures in some cases.[22–25] Thus, the sol–gel auto combustion route may be an optimal one, producing highly pure and uniform particles,[26] as heat treatment has also been shown to be a key factor for the evolution of the physical properties of this material, as proved by N. Pathak *et al.*[12]

Therefore, to obtain a high-performance and stable $ZnAl_2O_4$ material, it is important to carefully control the synthesis conditions to ensure lower energy and material loss.

Accordingly, the aim of this study is to combine these favourable conditions to obtain high-performance, stable and reproducible $ZnAl_2O_4$ nanoparticles by a sol–gel auto-combustion process to be used in several applications. In order to better understand the key issues involved in the process, the structural properties and morphology of the

---

[a] *Laboratory of Applied Physics, Faculty of Sciences of Sfax, University of Sfax, B. P. 1171, Sfax, 3000, Tunisia. E-mail: amirabougoffa@gmail.com; Tel: +216 26 923 772*
[b] *Laboratory of Spectroscopic Characterization and Optic Materials, University of Sfax, Faculty of Sciences of Sfax, B. P. 1171, 3000 Sfax, Tunisia*
[c] *University of Coimbra, CFisUC, Physics Department, Rua Larga, P-3004-516 Coimbra, Portugal*

prepared powder were evaluated at room temperature by the XRD technique and TEM, respectively. In addition, the vibrational and optical properties were investigated by RAMAN and UV-visible spectroscopies carried out at room temperature. Then, the luminescent properties of the synthesized material were examined by photoluminescence (PL) spectroscopy. Finally, the electrical properties of $ZnAl_2O_4$ were investigated at different temperatures from 60 to 380 K at a frequency range of 0.1 Hz to 1 MHz.

2. Experimental methods and tools

2.1. Sol–gel auto-combustion process

The $ZnAl_2O_4$ material was synthesized by the sol–gel auto-combustion method. First, zinc oxide (ZnO, 98% purity), dissolved in nitric acid, and aluminum nitrate ($Al(NO_3)_3 \cdot 9H_2O$, 98% purity) were used as the initial precursors. Then, the obtained powder was crushed and calcined at 700 °C for 6 hours. Finally, this operation was repeated with an annealing temperature of 900 °C for 24 hours to enhance the crystallinity of the prepared powders.

After the annealing process, the obtained powder was pressed into pellets 8 mm in diameter, and annealed at 700 ℃ for 2 hours. The bulk density of the obtained pellet was estimated to be 3.61 g cm^{-3} according to the following expression:[27]

$$\rho = \frac{m}{\pi r^2 h}$$

where h, m and r are, respectively, the thickness, the mass and the radius of the pellet.

2.2. Measurements tools

The phase and structure of the $ZnAl_2O_4$ powder were examined by X-ray Diffraction (XRD) using a Bruker 8D Advance X-ray powder diffractometer, with CuKα1 radiation (λ = 1.5406 Å). Raman and UV-vis properties were measured using an HR 800, Jobin Yvon and Varian Cary 5000 UV-Vis-NIR spectrometer, respectively. Photoluminescence (PL) emission spectra were measured in the wavelength range of 250–850 nm using a Horiba Jobin Yvon fluorolog-3 spectrofluorometer with an excitation wavelength of 260 nm. For the electrical measurements, the back and front surfaces of the produced pellet were masked with a thin gold layer and then the sample was fixed between two copper electrodes in a special holder. After that, measurements were carried out by impedance spectroscopy in the temperature range of 40–380 K at a frequency range of 0.1 Hz to 1 MHz using an Agilent 4294 analyzer.

3. Results

3.1. XRD measurements

The crystalline structure and the purity of the synthesized $ZnAl_2O_4$ powder were evaluated by X-ray diffraction (XRD) measurement recorded at room temperature. The obtained XRD pattern was refined with the FULLPROF Rietveld program,[28,29] proving the normal spinel cubic structure with the $Fd\bar{3}m$ space group where the zinc and aluminate cations occupy their normal positions (Zn occupies the tetrahedral site and Al occupies the octahedral site). The observed and calculated patterns of the prepared $ZnAl_2O_4$ sample as well as the Bragg positions are displayed in Fig. 1. As a result, the structural parameters deduced from the pattern refinement are provided in Table 1.

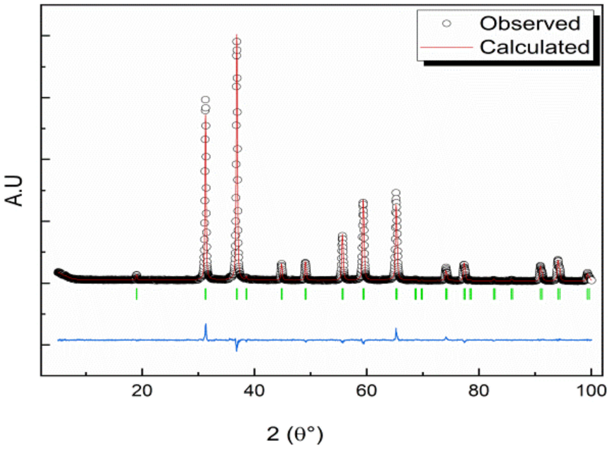

Fig. 1 Refined XRD pattern of the $ZnAl_2O_4$ material.

Table 1 Structural parameters of the refined normal spinel structure of the $ZnAl_2O_4$ material

Space group			$Fd\bar{3}m$
a			8.085160
$\chi 2$			2.45
R_p			11.6
R_{wp}			10.8
Atom positions			
	X	Y	Z
Zn	0.12500	0.12500	0.12500
Al	0.50000	0.50000	0.50000
O	0.26532	0.26532	0.26532

Assuming that the contributions of particle size and lattice strain to the line broadening are independent of each other, the observed line width is simply the sum of these two contributions, leading to the Williamson–Hall equation:[30]

$$\beta \cos \theta = \frac{K\lambda}{D_{WH}} + 4\varepsilon \sin \theta$$

Therefore, the plot of $(\beta \cos \theta)$ as a function of $(4 \sin \theta)$ is displayed in Fig. 2. Then, the average value of the crystallite size, D_{WH} was deduced from the intercept and slope of the fitted line to be 36 nm.

3.2. Morphology

TEM and SEM were used to evaluate the morphology, shape and size distribution, and to assess the degree of agglomeration of

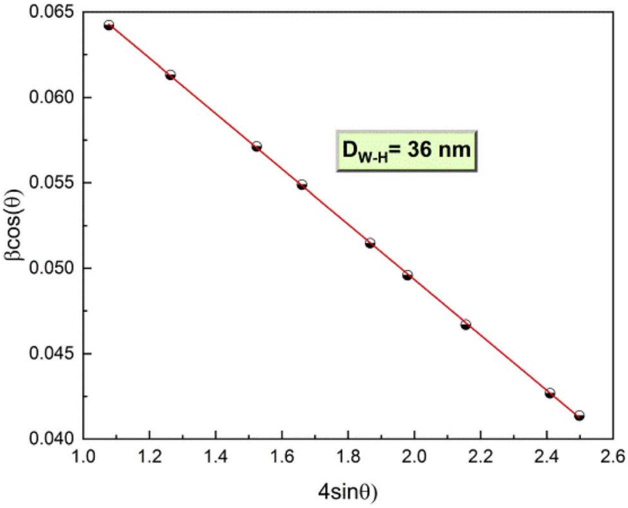

Fig. 2 The plot of ($\beta \cos \theta$) as a function of ($4 \sin \theta$) according to the Williamson–Hall model.

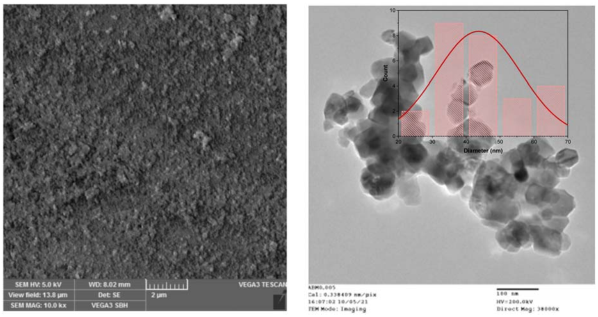

Fig. 3 SEM image, TEM image and grain size histogram of the $ZnAl_2O_4$ nanopowder.

the prepared powder. The obtained TEM image presented in Fig. 3 indicates the existence of agglomerations, composed of fine crystallites with semi-spherical shapes about 45 nm in size, as proved by the grain size histograms based on manual statistical particle size analysis performed using Image-J software displayed in the same figure.

3.3. Raman spectroscopy

Fig. 4 presents the RAMAN spectra of the synthesized $ZnAl_2O_4$. According to group theory, the normal spinel structure known as the Gahnite structure presents five Raman active modes: A1g + Eg + 3T2g. As observed in Fig. 4, only two modes are detected at 420 cm^{-1} and 661 cm^{-1} attributed to the Eg and the T2g mode, respectively, as observed previously.[31]

Indeed, the higher-frequency T2g mode is due to the motions of oxygen atoms (breathing mode) inside the AlO_6 octahedra. It is also important to mention that the inexistence of a vibration mode at around 727 cm^{-1} of the AlO_4 tetrahedra,[31] attributed to structural disorder, indicates that no inversion was detected in the studied spinel structure. Thus, the Eg band at 420 cm^{-1} does not prove the asymmetric behavior of the disordered spinel, confirmed by a Gaussian curve with an R^2 of 0.996. These results are in good agreement with the Rietveld refinement, proving a normal spinel structure.

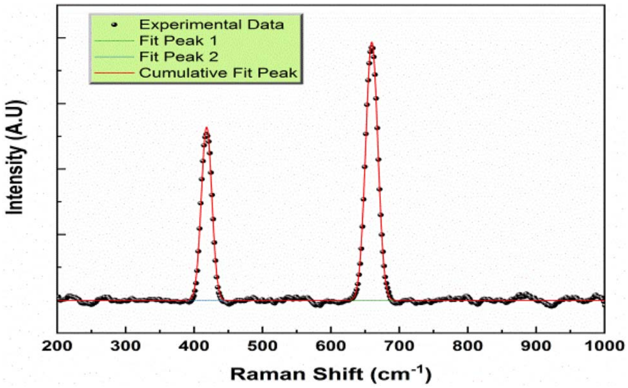

Fig. 4 Fitted RAMAN spectrum of the $ZnAl_2O_4$ material.

3.4. Optical investigation

3.4.1. UV-visible spectroscopy and DFT calculations. The UV-visible diffuse reflectance spectra of the $ZnAl_2O_4$ sample recorded at room temperature in the wavelength range of 200–900 nm have been used to estimate the absorption coefficient (α) based on Kubelka–Munk function $F(R)$ given as:[32]

$$F(R) = \frac{(1 - R_\infty)^2}{2R_\infty} \approx \alpha$$

where R_∞ represents the diffuse reflectance of the sample with infinite thickness.

Therefore, we have plotted in Fig. 5, the variation of $(F(R)h\nu)^2$ as a function of the energy ($h\nu$) in order to estimate the band gap of the synthesized $ZnAl_2O_4$ material. The obtained plot indicates the existence of two bands at about 1.5 eV and 2.5 eV that are due to the existence of defects and vacancies in the prepared sample, knowing that this material has a gap energy that can reach 4.5 eV as reported in several research works.[33–35]

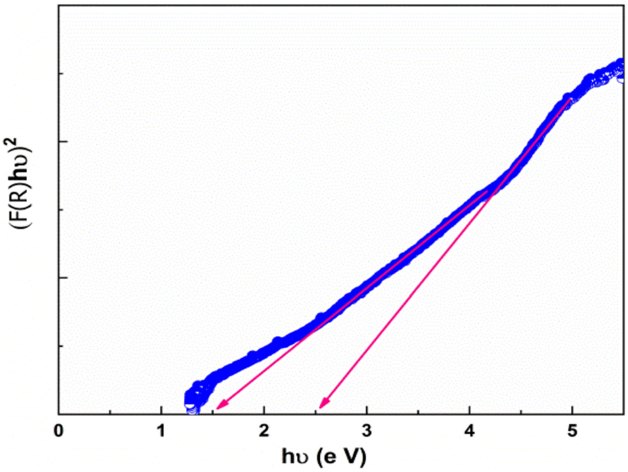

Fig. 5 Variation of the $(F(R)h\nu)^2$ *versus* $h\nu$ Tauc plots of the $ZnAl_2O_4$ material.

Accordingly, in order to discuss the possible factors responsible for this observation and provide a qualitative insight into the electronic structure of $ZnAl_2O_4$ with vacancy defects, we have used density functional theory (DFT). In particular, the possible emergence of defect-induced in-gap states associated with oxygen and zinc vacancies can support the interpretation of the experimental observations by identifying defect states that may be the origin of the observed PL emission and optical transitions. The present DFT calculations, performed within the GGA-PBE approximation, were carried out using the WIEN2k simulation package to simulate the effect of oxygen and zinc vacancies on the band diagram of the $ZnAl_2O_4$ material referring to the investigation of S. Huang *et al.*[22]

Accordingly, the experimental structural parameters obtained from Rietveld refinement were employed to perform the numerical study of $ZnAl_2O_4$. To model the $Zn_{0.75}Al_2O_{3.75}$ composition, two Zn atoms and two oxygen atoms were removed from the parent $ZnAl_2O_4$ structure. The convergence criteria were set to an energy threshold of 10^{-4} Ry and a force threshold of 10^{-3} Ry·Å^{-1}.

The obtained Band diagram and DOS structure of $ZnAl_2O_4$ and $Zn_{0.75}Al_2O_{3.75}$ are illustrated in Fig. 6 and 7, respectively. These findings confirm that the existence of Zn and O vacancies can create levels in the band gap of $ZnAl_2O_4$ and be responsible for the observation of several transitions as observed in Fig. 5.

The obtained results present an agreement with previous theoretical studies on defected oxide materials.[36] However, it is well established that standard DFT approaches tend to underestimate the band gap due to intrinsic limitations of approximate exchange–correlation functionals.[37–39] In addition, these methods do not explicitly include many-body effects, excitonic interactions, or electron–phonon coupling, which play a crucial role in optical processes such as photoluminescence.[40,41]

3.4.2. Pl investigation. The room temperature PL spectrum of the $ZnAl_2O_4$ material, displayed in Fig. 8, proves different peaks at different wavelengths in the ultraviolet-visible-near-infrared region (UV-visible-NIR) located at $\lambda = 385$ nm, blue at $\lambda = 458$ nm, green at $\lambda = 524$ nm, red at $\lambda = 712$ nm, and NIR at $\lambda = 766$ nm. This observation proves the presence of various electronic states in the band gap, where each color is due to a specific electronic transition. These important findings are obtained without doping the $ZnAl_2O_4$ material. This proves that the synthesis and heat conditions that differ between research studies can also impact the optical properties of materials for this reason its should be carefully controlled.

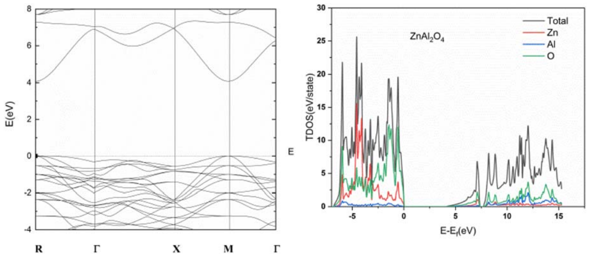

Fig. 6 Band diagram and DOS structure of the $ZnAl_2O_4$ material.

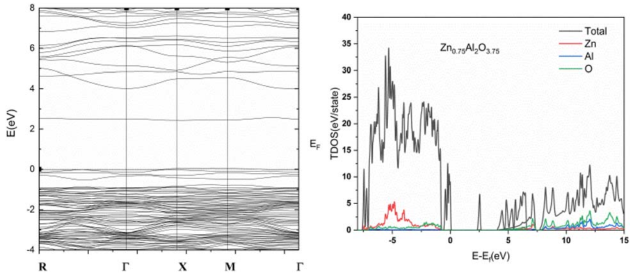

Fig. 7 Band diagram and DOS structure of the $Zn_{0.75}Al_2O_{3.75}$ material.

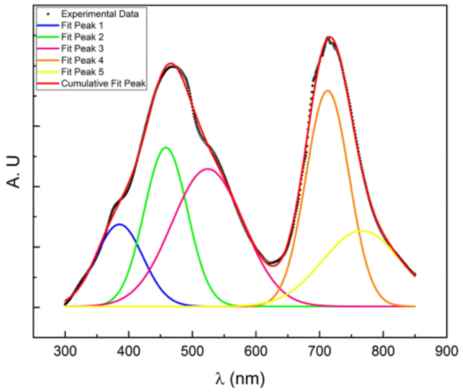

Fig. 8 PL emission spectra of the $ZnAl_2O_4$ material with excitation at $\lambda = 260$ nm.

The observed emission at 385 nm could be due to shallow level O-vacancy defect vacant states below the CB and some filled states just above the VB. On the other hand, in an earlier work, the authors attributed emissions at 450 nm to oxygen vacancies.[22] The 524 nm emission could be related to the transition from the Zn vacancy level (VZn) to the oxygen vacancy level (VO).[35] However, the near-infrared band located at 712 nm and 766 nm could either be the result of the transition from the bottom level of the $ZnAl_2O_4$ conduction band to the O vacancy (VO) level, or the transition from the O vacancy (VO) level to the valence band top.[35] These results are confirmed with good agreement with the DFT calculation results presented in Fig. 6 and 7.

3.5. Electrical investigation

Fig. 9a, shows the dependence of the DC conductivity of the $ZnAl_2O_4$ sample on the inverse of temperature according to the proposed theories of Mott.

Fig. 9a proves that the conductivity is found to be lower at low temperatures and increases with at temperature increasing, indicating a thermally activated DC conductivity. Indeed, this thermal activation is assisted by the SPH conduction process at high temperatures with an activation energy of about 96 meV, where the transport of charge carriers is due to a phonon-assisted hopping process of polarons between localized states.[42–45] However, at lower temperatures, the conduction process is governed by an activated VRH conduction process,

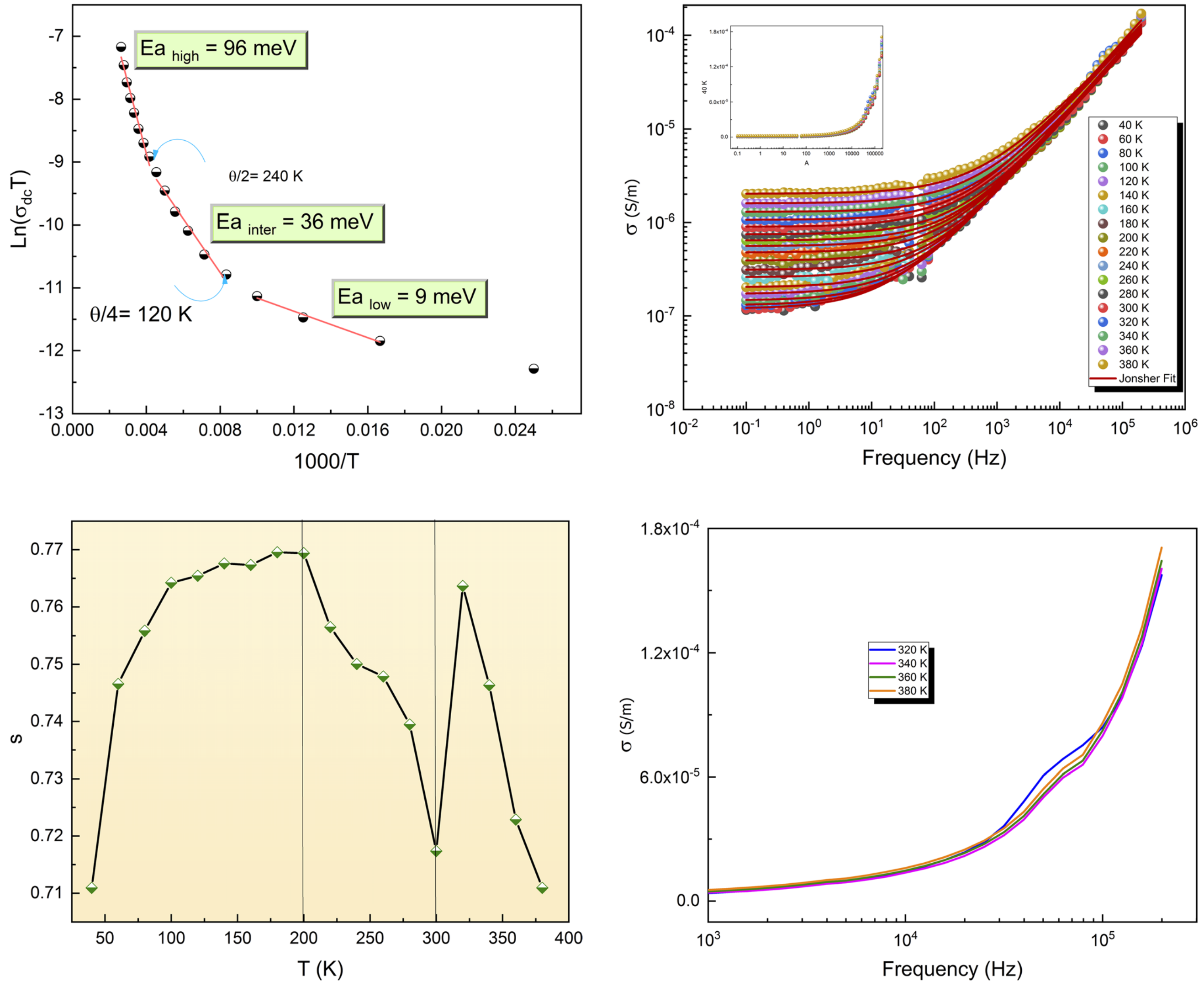

Fig. 9 (a) $\ln(\sigma_{dc}T)$ as a function of $1000/T$ according to the Mott model. (b) Theoretical adjustment of (σ_{ac}) as a function of frequency according to the Jonscher model. (c) Temperature dependence of the s exponent. (d) Effect of temperature on the conductivity of the $ZnAl_2O_4$ material.

with an activation energy of about 9 meV, characterized by negligible hopping and binding energies according to Mott predictions.[42–45]

The plot of $\ln(\sigma_{dc})$ *versus* $1/(T^2)$ displayed in the inset of Fig. 9a was fitted according to the following expression:[42–45]

$$\sigma_{dc} = \sigma_0 e^{\left(-\frac{T_0}{T}\right)^{0.25}}$$

where σ_0 is a pre-exponential factor.

Therefore, the deduced T_0 was used to estimate the density of localized states at the Fermi level and $N(E_F)$ according to the following expression:[27]

$$T_0 = \frac{3\alpha^3 2^{\frac{1}{4}}}{2\pi k_B N(E_F)}$$

where α presents the decay factor of the localized wave function and $1/\alpha$ is estimated as the Bohr radius of the localized center ($r_B = 0.83$ Å).[46]

The obtained $N(E_F)$ is about 2.4×10^{25} eV^{-1} cm^{-1}, presenting a high value compared to other spinel structured materials.[27,47] This result can confirm the attribution of the multicore PL emissions to the existence of defects in the studied structure. On the other hand, the frequency dependence of the semi-log plot of electrical conductivity under a large variation of temperature is shown in Fig. 9b. By observing this figure, we can clearly distinguish the semiconductor behavior of the conductivity with respect to the frequency, which can be composed of two parts following the Jonscher power law.

Indeed, the observed plateau-type behavior in the low frequency region corresponds to the direct current conductivity σ_{dc} and is interrelated with the long-range translational motion of charge carriers. Then, at high frequencies, a clear dispersion was distinguished derived from the relaxation of the ionic atmosphere after the movement of particles and obeys the universal power law $A\omega^s$.[48]

Accordingly, the total ac conductivity, σ_{ac}, can be investigated by theoretical adjustment using the following Jonscher's power law:[48]

$$\sigma_{ac} = \sigma_{dc} + A\omega^{s}$$

where A is the temperature dependent pre-exponent factor, ω is the angular frequency, and s is the power law exponent, representing the degree of interaction between the mobile charge carriers and their surrounding lattices.

To explain the carrier transport and identify the conduction mechanism in such materials, researchers have classically referred to the hopping over a barrier and quantum–mechanical tunneling processes that can be assisted either by electrons, polarons, ions or atoms.[49] Moreover, the transport of charge carriers in these materials is conventionally explained according to the evolution of the frequency exponent "s" *versus* temperature, presenting then a necessary analysis to identify the conduction process. Generally, this latter is governed by the CBH, OLPT and NSPT models, where "s" is temperature dependent and $0 < s < 1$, or the QMT one described by a constant value of about 0.8 regardless of the temperature.[50]

Furthermore, the variations of the "s" parameter shown in Fig. 9c indicate a correlated barrier hopping (CBH) conduction process at a lower temperature and a small polaron tunnel (NSPT) one at high temperatures with a remarkable perturbation after $T = 320$ K, as also observed in the conductivity plots displayed in Fig. 9d.

Concerning the CBH conduction mechanism, the charge carrier hopping among site pairs occurs over a potential barrier where the "s" exponent decreases with temperature as follows:[50]

$$s = 1 - \frac{6k_BT}{(W_M + k_BT\ln(2\pi f\tau_0))}$$

where τ_0 is the characteristic relaxation time, k_B is the Boltzmann constant and W_M is the hopping energy.

However, in the NSPT model, the increase of the "s" exponent with temperature is described by the following relation:[50]

$$s = 1 + \frac{4k_BT}{(W_M - k_BT\ln(2\pi f\tau_0))}$$

4. Conclusions

In this study, the synthesis of $ZnAl_2O_4$ nanopowder by an auto-combustion route leads to a normal spinel $Fd\bar{3}m$ cubic structure as confirmed by RAMAN spectra recorded at room temperature and exhibiting two peaks corresponding to Eg and T2g modes. The morphology of the prepared powder evaluated by TEM microscopy proves the existence of semi-spherical particles with a size about 45 nm. The optical properties and PL emission spectra exhibit multicolor emission that can be attributed to defects and vacancies in the material. Finally, the investigation of the electrical properties of the synthesized $ZnAl_2O_4$ proves that it exhibits a semiconductor behavior following the Jonscher law. All of the results present a good agreement and indicate the promise of $ZnAl_2O_4$ materials for electronic and optoelectronic applications.

Author contributions

The manuscript was written through contributions of all authors. All authors have given approval to the final version of the manuscript. Amira Bougoffa: sample synthesis, conceptualization, methodology, writing, original draft preparation. Ala Eddin Mabrouki: investigation, visualization, DFT calculations, writing. Adel Benali: optical measurements and methodology. Essebti Dhahri: review, editing, methodology and validation. Abderrazek Oueslati: dielectric measurements and methodology. B. F. O. Costa: data curation and validation.

Conflicts of interest

The authors declare that there is no conflict of interest.

Data availability

All data relevant to this study are available from the corresponding author upon reasonable request.

References

1 I. A. Denisov, Y. V. Volk, A. M. Malyarevich, K. V. Yumashev, O. S. Dymshits, A. A. Zhilin and K. H. Lee, *J. Appl. Phys.*, 2003, **93**, 3827–3831.
2 Y. Xu, P. Fu, B. H. Zhang, J. Gao, L. Zhang and X. H. Wang, *Mater. Lett.*, 2014, **123**, 142–144.
3 A. D. Ballarini, S. A. Bocanegra, A. A. Castro, S. R. De Miguel and O. A. Scelza, *Catal. Lett.*, 2009, **129**, 293–302.
4 P. Bhavani, A. Manikandan, P. Paulraj, A. Dinesh, M. Durka and S. A. Antony, *J. Nanosci. Nanotechnol.*, 2018, **18**, 4072–4081.
5 W. N. Wan Jalal, H. Abdullah, M. S. Zulfakar, B. Bais, S. Shaari and M. T. Islam, *Trans. Indian Ceram. Soc.*, 2013, **72**, 215–224.
6 L. Cornu, M. Gaudona and V. Jubera, *J. Mater. Chem.*, 2013, **1**, 5419–5428.
7 K. E. Sickafus, J. M. Wills and N. W. Grimes, *J. Am. Ceram. Soc.*, 1999, **82**, 3279–3292.
8 X. L. Zhu, Z. Q. Wei, W. H Zhao, X. D Zhang, L. Zhang and X. Wang, *J. Electron. Mater.*, 2018, **47**, 6428–6436.
9 X. L. Zhu, Z. Q. Wei, W. H. Zhao, X. D. Zhang, X. J. Wu and J. L. Jiang, *Curr. Nanosci.*, 2018, **14**, 474–480.
10 L. Zhang, G. F. Ji, F. Zhao and Z. Z. Gong, *Chin. Phys. B*, 2011, **20**, 412–418.
11 G. Cabello, L. Lillo, C. Caro, M. Seguel, C. Sandoval, G. E. Buono-Core and M. Flores Carrasco, *Mater. Res. Bull.*, 2016, **77**, 212–220.
12 N. Pathak, S. K. Gupta, K. Sanyal, M. Kumar, R. M. Kadam and V. Natarajan, *Dalton Trans.*, 2014, **43**, 9313–9323.
13 S. Singh and K. Pal, *Mater. Sci. Eng., A*, 2015, **644**, 325–336.
14 H. Y. Yue, W. D. Fei and L. D Wang, *J. Mater. Sci.*, 2008, **43**, 6233–6237.

15 W. M. Mulwa, B. F. Dejene, M. O. Onani and C. N. M. Ouma, *J. Lumin.*, 2017, **184**, 7–16.

16 T. Sofia Nirmala, N. Iyandurai, S. Yuvaraj and M. Sundararajan, *Mater. Res. Express*, 2020, **7**, 4.

17 T. Tangcharoen, J. T. Thienprasert and C. Kongmark, *Int. J. Appl. Ceram. Technol.*, 2021, **18**, 1125–1143.

18 K. K. Kumar, T. S. Kumar, B. R. Reddy, C. S. Chakra, K. Praveena, S. Katlakunta and J. Sol, *Gel Sci. Technol.*, 2024, **111**, 794–805.

19 B. Goswami, G. Rani and R. Ahlawat, *Phys. Scr.*, 2023, **98**(11), 115974.

20 S. Yuvaraj, S. Ramachandran, A. Subramani, A. Thamilselvan, S. Venkatesan, M. Sundararajan and C. S. Dash, *J. Supercond. Nov. Magn.*, 2020, **33**, (4), 1199–1206, https://www.sciencedirect.com/science/article/pii/S2949822825007555.

21 N. M. Gahane, P. J. Chaware and K. G. Rewatkar, *Int. J. Chem. Math. Phys.*, 2023, **7**(1), 1–6.

22 Sh. Huang, Z. Wei, X. Wu and J. Shi, *J. Alloys Compd.*, 2020, **825**, 154004.

23 L. N. Adoons, T. A. Nhlapo, T. Molefe, L. Kotsedi, A. U. Yimamu, T. P. Mokoena, D. Ntshalintshali and M. Malimabe, *Next Mater.*, 2025, **9**, 101237.

24 V. Cabuil, V. Dupuis, D. Talbot and S. Neveu, *J. Magn. Magn. Mater.*, 2011, **323**, 1238–1241.

25 M. Eshraghi and P. Kameli, *Curr. Appl. Phys.*, 2011, **11**, 476–481.

26 S. T. Aruna and A. S. Mukasyan, *Curr. Opin. Solid State Mater. Sci.*, 2008, **12**, 44.

27 A. Slimani, A. Bougoffa, R. Dhahri, M. Krichen, E. Dhahri and B. F. O. Costa, *J. Alloys Compd.*, 2026, **1057**, 186729.

28 H. M. Rietveld, *J. Appl. Crystallogr.*, 1965, **2**, 65.

29 R. A. Young, *The Rietveld Method*, Oxford University Press, New York, 1993.

30 A. Guinier and I. Dunod, *Theorie et Technique de la radiocristallographie*, 3rd edn, vol. 462, 1964.

31 D. Simeone, C. Dodane-Thiriet, D. Gosset, P. Daniel and M. Beauvy, *J. Nucl. Mater.*, 2002, **300**, 151–160.

32 R. Ahsan, M. Z. Rahman Khan and M. Abdul Basith, *J. Nanophotonics*, 2017, **11**(4), 046016.

33 K. Kumar, K. Ramamoorthy, P. M. Koinkar, R. Chandramohan and K. Sankaranarayanan, *J. Nanopart. Res.*, 2007, **9**, 331–335.

34 A. Chaudharya, A. Mohammad and S. M. Mobina, *Mater. Sci. Eng., B*, 2018, **227**, 136–144.

35 N. Pathak, P. Sarathi Ghosh, S. Saxena, D. Dutta, A. Kumar, D. Bhattacharyya, S. N. Jha and R. M. Kadam, *Inorg. Chem.*, 2018, **57**(7), 3963–3982.

36 C. Freysoldt, B. Grabowski, T. Hickel, *et al.*, First-principles calculations for point defects in solids, *Rev. Mod. Phys.*, 2014, **86**, 253.

37 J. P. Perdew, K. Burke and M. Ernzerhof, Generalized Gradient Approximation Made Simple, *Phys. Rev. Lett.*, 1996, **77**, 3865.

38 J. P. Perdew and M. Levy, Physical content of the exact Kohn–Sham orbital energies, *Phys. Rev. Lett.*, 1983, **51**, 1884.

39 A. J. Cohen, P. Mori-Sánchez and W. Yang, Insights into current limitations of density functional theory, *Science*, 2008, **321**, 792.

40 G. Onida, L. Reining and A. Rubio, Electronic excitations: density-functional *versus* many-body Green's-function approaches, *Rev. Mod. Phys.*, 2002, **74**, 601.

41 F. Bechstedt, *Many-body Approach to Electronic Excitations*, Springer, 2015.

42 N. F. Mott, Conduction in glasses containing transition metal ions, *J. Non-Cryst. Solids*, 1968, **1**(1), 1.

43 I. G. Austin and N. F. Mott, Polarons in crystalline and non-crystalline materials, *Adv. Phys.*, 1969, **18**(71), 41.

44 N. F. Mott, Conduction in non-crystalline materials, *Philos. Mag.*, 1969, **19**(160), 835.

45 N. F. Mott, Polarons, *Mater. Res. Bull.*, 1978, **13**(12), 1389.

46 C. Godet, *Phys. Status Solidi B*, 2002, **231**, 499–511.

47 A. Hadded, J. Massoudi, E. Dhahri, K. Khirouni and B. F. O. Costa, *RSC Adv.*, 2020, **10**, 42542–42556.

48 A. K. Jonscher, *Universal Relaxation Law*, Chelsea Dielectric Press, London, 1996.

49 N. F. Mott, *Philos. Mag.*, 1969, **19**(160), 835.

50 Y. Moualhi, H. Rahmouni and K. Khirouni, *Results Phys.*, 2020, **19**, 103570.